Valley and spin splittings in PbSe nanowires

I. D. Avdeev,[1] A. N. Poddubny,[1] S. V. Goupalov,[1,2] and M. O. Nestoklon[1]
[1]*Ioffe Institute, St. Petersburg 194021, Russia*
[2]*Department of Physics, Jackson State University, Jackson Mississippi 39217, USA*
(Received 25 May 2017; published 25 August 2017)

We use an empirical tight-binding approach to calculate electron and hole states in [111]-grown PbSe nanowires. We show that the valley-orbit and spin-orbit splittings are very sensitive to the atomic arrangement within the nanowire elementary cell and differ for [111] nanowires with microscopic D_{3d}, C_{2h}, and D_3 symmetries. For the nanowire diameter below 4 nm the valley-orbit splittings become comparable with the confinement energies and the $\boldsymbol{k}\cdot\boldsymbol{p}$ method is inapplicable. Nanowires with the D_3 point symmetry having no inversion center exhibit giant spin splitting $E=\alpha k_z$, linear in one-dimensional wave vector k_z, with the constant α up to 1 eV Å.

DOI: 10.1103/PhysRevB.96.085310

I. INTRODUCTION

Lead chalcogenide nanostructures are widely used for optoelectronics applications, including infrared detectors [1], solar cells [2,3], and light emitting diodes [4,5]. Most of the works are devoted to zero-dimensional nanocrystals [1–6]. However, quasi-one-dimensional lead chalcogenide nanowires (NWs) and nanorods are offering more flexibility. In particular, enhanced multiple exciton generation efficiency [7–10] and suppressed Auger recombination rates [11–13] have been experimentally demonstrated in PbSe NWs. PbSe NWs can be grown using methods of colloidal chemistry [14–19]. The approach based on the oriented attachment of PbSe nanocrystals [15] enables controllable growth of NWs along the [100], [110] and [111] axes with straight, zigzag, helical, branched, and tapered shape. Growth of high-quality monocrystalline PbSe [100] nanorods with homogeneous size distributions using a catalyst-free, one-pot, solution chemistry method has been reported in Refs. [16,17]. This technique offers control over the nanorod aspect ratio in the range from 1–16 [18,19]. The energy spectrum of the nanowires can be probed optically [17,20–22]. Simple stationary linear absorption spectroscopy easily probes the effect of the nanorod size [21] and aspect ratio [18] on the fundamental energy gap. More detailed information might be accessible using the nonlinear and transient optical setups [22,23].

While the basics of the electron structure of the nanowires is well understood, the valley structure of the states has not been fully investigated. The multivalley band structure represents a challenge for the modeling, as one has to deal with electronic states, originating from different valleys, whose degeneracies are very sensitive to the microscopic properties and symmetry of a nanostructure. The symmetry of a nanowire made of a crystalline material with the rocksalt crystal lattice, having band extrema in four L points of the Brillouin zone, is determined by several major factors.

The first of these factors is the nanowire growth direction. In most theoretical papers [20,24], NWs grown along the two high-symmetry directions, [100] and [111], are considered. Theoretical works based on the effective mass method [20,25,26] treat the valleys as independent. However, if the valley mass anisotropy is taken into account [20], this description becomes sensitive to the growth direction. In the absence of intervalley coupling, the electronic states in [100] NWs remain fourfold valley degenerate while in [111] NWs the longitudinal [111] valley state becomes split off by the effective mass anisotropy.

The second factor is the shape of the NW cross section. For a theoretical model, it is natural to choose it in such a way that it does not reduce the overall symmetry of the nanowire. The simplest choice is the shape, which is as close to a circle as possible. The presence of the NW surface leads to mixing of the valley states (intervalley coupling), which results in energy splittings [27–32]. The structure of electron energy levels resulting from the valley splittings may be determined from the overall nanowire symmetry, which is the combination of the O_h symmetry of the crystal lattice and the symmetry of the NW structure potential. The effective mass method may be extended to account for the valley degree of freedom, so that it can be used to predict the degeneracies of resulting energy eigenstates and their transformation properties. Such an extension of the effective mass method and symmetry analysis of the intervalley coupling is one of the aims of the present paper. However, a full quantitative analysis of the intervalley coupling requires computational methods capable of accounting for the atomistic structure of the nanowire. Below we employ the empirical tight-binding method to perform such an analysis. This method has proved to be effective in the description of the intervalley coupling in lead chalcogenide nanocrystal quantum dots [33] and in nanowires with a rectangular cross section [24]. Contrary to *ab initio* techniques [34,35], that are as yet limited to the NWs thinner than 30 Å [34,35], the tight-binding method can easily handle NWs with large diameters. An empirical tight-binding description also naturally accounts for the relativistic nature of Pb atoms that induces strong spin-orbit interaction, representing a challenge for the *ab initio* approaches [36,37].

Even when the nanowire growth direction and the shape of its cross section are chosen, the symmetry of the nanowire is not fully determined. For a nanowire with a cylindrical shape, the position of the axis of this cylinder within a unit cell of a bulk semiconductor is yet to be specified. It turns out that not only is the intervalley coupling sensitive to the choice of this position, but entirely new physical consequences such as appearance of spin-dependent splittings of nanowire energy levels can also result. From this point of view, the [111]-grown NWs appear to be more interesting, and we will restrict our consideration to these NWs. Analysis of the [100]-grown NWs is a topic for future research.

The paper is organized as follows. In Sec. II we describe the system and explain the microscopic symmetry of the NWs. In Sec. III we describe the extension of the effective mass method that takes into account combinations of the valley states. We formally consider an ideal cylindrical nanowire, but restrict ourselves to the symmetry operations of the true nanowire symmetry group specified in Sec. II. This allows us to predict the degeneracies of eigenenergies and transformation properties of eigenfunctions resulting from the valley-orbit and spin-orbit splittings. In Sec. IV we explain the tight-binding approach and its application to lead chalcogenides NWs. We describe a technique for detailed analysis of the tight-binding wave functions in both real and reciprocal spaces. In Sec. V we discuss the results of the tight-binding calculations and compare them with the effective mass consideration. In Sec. VI the conclusions are drawn.

II. WIRE STRUCTURE IN REAL AND RECIPROCAL SPACES

In this section we analyze the possible microscopic symmetries of the PbSe nanowires grown along the [111] direction. Bulk PbSe has the rocksalt (fcc) crystal lattice with the O_h point group. An elementary cell of a NW grown along [111] direction contains three Pb and three Se (111) atomic layers, as shown in Fig. 1. NWs have one-dimensional (1D) periodicity along the growth direction characterized by the translational vector

$$\boldsymbol{T} = a(1,1,1), \tag{1}$$

where a is the PbSe lattice constant. A nanowire is carved out of the bulk crystal along a cylindrical surface with an axis parallel to the [111] direction. Some possible arrangements of atoms in the elementary cells of resulting nanowires are shown in Fig. 1. They differ by the position of the NW axis with respect to the unit cell of a bulk crystal leading to different point symmetries of the resulting NWs. In particular, Fig. 1 shows three typical NWs with the center axis passing through the atom [D_{3d}, Fig. 1(a)], between atoms [D_3, Fig. 1(b)] or through the middle of a chemical bond [C_{2h}, Fig. 1(c)]. In the case of the D_{3d} NWs we choose the inversion center at the (0,0,0) cation. For the C_{2h} NWs, the inversion center is chosen at $a(\frac{1}{2},\frac{1}{4},\frac{1}{4})$. Note that the crystallographic coordinate system is used only to define NW directions, their inversion centers, and reciprocal lattice vectors. Below we use the coordinate system with the following axes:

$$\boldsymbol{x} \parallel [\bar{1}10], \quad \boldsymbol{y} \parallel [\bar{1}\bar{1}2], \quad \boldsymbol{z} \parallel [111] \tag{2}$$

and, for the D_{3d} and C_{2h} NWs, the origin of this coordinate system is set to the inversion center.

Now we discuss the relations between the one-dimensional reciprocal space of a nanowire and the three-dimensional reciprocal space of the parent bulk material. The conduction band minima and valence band maxima in bulk lead chalcogenides are located in the four inequivalent L valleys. The first Brillouin zone is schematically shown in Fig. 1(d). The point group of the wave vector in each L valley is D_{3d} with its C_3 axis directed along the valley. Four valleys L_ν correspond to the wave vectors $\boldsymbol{k}_\nu$ ($\nu = 0,1,2,3$), which we choose as

$$\boldsymbol{k}_0 = \frac{\pi}{a}(1, \quad 1, \quad 1), \quad \boldsymbol{k}_1 = \frac{\pi}{a}(-1, -1, \quad 1),$$
$$\boldsymbol{k}_2 = \frac{\pi}{a}(1, -1, -1), \quad \boldsymbol{k}_3 = \frac{\pi}{a}(-1, \quad 1, -1). \tag{3}$$

We also choose the basis vectors of the bulk reciprocal lattice as

$$\boldsymbol{b}_1 = -2\boldsymbol{k}_3, \quad \boldsymbol{b}_2 = -2\boldsymbol{k}_1, \quad \boldsymbol{b}_3 = -2\boldsymbol{k}_2. \tag{4}$$

In the one-dimensional reciprocal space of a nanowire, the quantum-confined states, originating from the electron and hole states at the L points in the 3D bulk Brillouin zone,

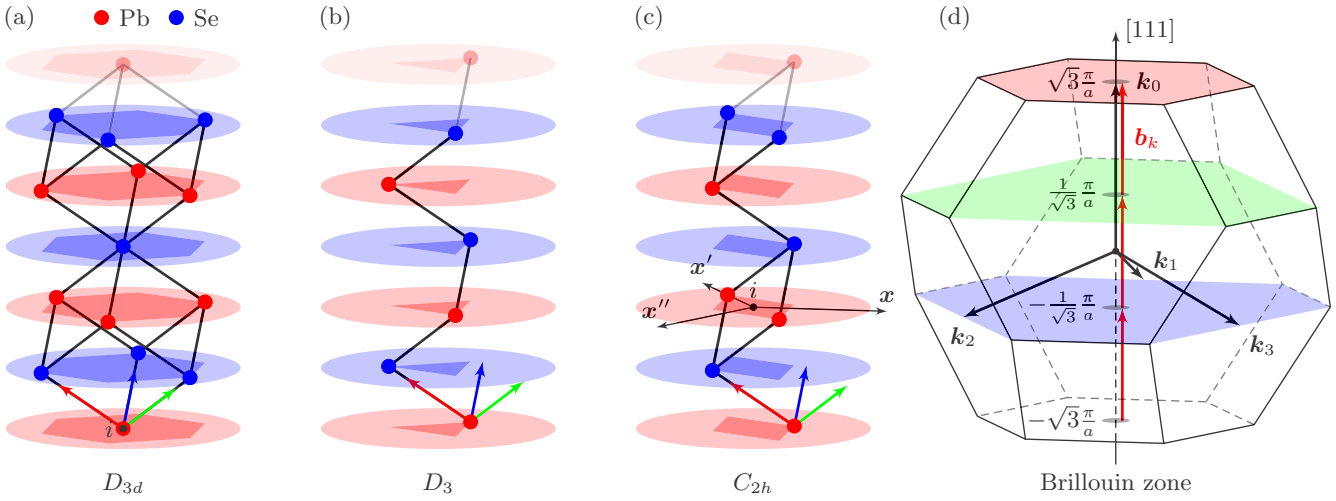

FIG. 1. (a)–(c) show elementary cells of three smallest NWs with the point group symmetry D_{3d}, D_3, and C_{2h}, respectively. Cations (Pb) are shown by red dots, and anions (Se) by blue dots. Color arrows (RGB for XYZ) indicate the crystallographic coordinate system with the origin at the point (0,0,0). Inversion center of the D_{3d} NW is at the (0,0,0) cation, while in the C_{2h} NW the inversion center is chosen at the $a(\frac{1}{2},\frac{1}{4},\frac{1}{4})$ point in the crystallographic coordinate system. Three auxiliary axes $\boldsymbol{x} \parallel [\bar{1}10]$, $\boldsymbol{x}' \parallel [0\bar{1}1]$, $\boldsymbol{x}'' \parallel [10\bar{1}]$ are shown in (c). (d) shows the bulk PbSe Brillouin zone. Wave vectors $\boldsymbol{k}_i$ (3) are shown as black arrows. The colored cross sections are formed by (111) planes, which pass through the points $\boldsymbol{k}_1$, $-\boldsymbol{k}_1$, $\boldsymbol{k}_0$. Projections of these vectors to the [111] axis are indicated by tick marks on the [111] axis.

are located at the projections of the $\boldsymbol{k}_v$ onto the wire one-dimensional Brillouin zone defined by the vector

$$\boldsymbol{b}_k = \frac{2\pi}{|T|}\frac{1}{\sqrt{3}}(1,1,1), \tag{5}$$

whose length $b_k = 2\pi/a\sqrt{3}$ is three times shorter than the length of the basis reciprocal lattice vectors.

To illustrate the relation between the 1D and 3D Brillouin zones, in Fig. 1(d) we show three 1D Brillouin zones embedded into the 3D bulk Brillouin zone by red arrows. The three cross-section planes, which cut the 3D Brillouin zone at the projections of the valleys $\pm\boldsymbol{k}_{0,1,2,3}$ onto the [111] axis are painted in Fig. 1(d) in red, green, and blue. The wave vectors $\boldsymbol{k}_{0,1,2,3}$ are shown by black arrows. The distance between the cross sections is equal to the length of the 1D Brillouin zone, which means that the states originating from the four inequivalent L valleys become equivalent in the [111] NWs.

It is convenient to map all the inequivalent L valleys into a single (111) plane. The natural choice is the plane passing through the $\boldsymbol{k}_0$ point. In order to map the valleys into this plane, we add the reciprocal lattice vectors $\boldsymbol{b}_1$ and $\boldsymbol{b}_2 + \boldsymbol{b}_3$ to the vectors from the green and blue planes in Fig. 1, respectively. Below we will adhere to this scheme and, instead of addressing vectors from the three planes confined within the first 3D Brillouin zone, we will use equivalent vectors from the single plane. The planar translation vectors can be expressed via the reciprocal lattice vectors

$$\boldsymbol{T}_1^{2D} = \boldsymbol{b}_1 - \boldsymbol{b}_2, \quad \boldsymbol{T}_2^{2D} = \boldsymbol{b}_3 - \boldsymbol{b}_2. \tag{6}$$

III. EFFECTIVE MASS APPROACH

The $\boldsymbol{k}\cdot\boldsymbol{p}$ effective mass model to describe the electron energy spectrum near the extrema of the conduction and valence bands in a given L valley of a bulk lead chalcogenide compound (PbS, PbSe, PbTe, etc.) was proposed by Dimmock and Wright [38]. The isotropic version of this method, which neglects the mass anisotropy was used to calculate the states in spherical nanocrystals [39], cylindrical nanowires [25], and cylindrical nanorods [26]. Bartnik *et al.* [20] applied an axially symmetric model, which may be obtained by averaging the mass anisotropy in the directions, perpendicular to the nanowire growth direction, to describe quantum confined states in NWs. In what follows we further extend this approach to account for the mixing of the valley states. This enables us to classify the electron states in a nanowire with a given point symmetry (cf. Fig. 1) with respect to their transformation properties.

Figure 2 qualitatively illustrates the degeneracies of the lowest electron levels in the conduction band of $D_{3(d)}$ and C_{2h} symmetry NWs grown along the [111] direction. At $k_z = 0$ the level is eightfold (4 valleys $\times$ 2 spin) degenerate within the isotropic effective mass model [25]. The axially symmetric effective mass model [20] partially lifts this degeneracy by splitting this level into the twofold degenerate level originating from the longitudinal L_0 valley and the sixfold degenerate level formed by the states from the inclined valleys. Both the symmetry analysis in the framework of the $\boldsymbol{k}\cdot\boldsymbol{p}$ method presented below and the tight-binding calculations show that the states originating from the three inclined valleys are further split into three twofold degenerate levels. We label them in accordance with the irreducible representations of the point group of a NW using the Koster notation [40].

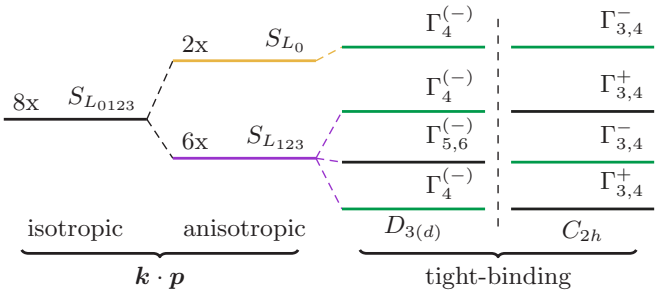

FIG. 2. Scheme of the lowest electron energy levels in $D_{3(d)}$ and C_{2h} [111]-grown NWs. Left to right: isotropic $\boldsymbol{k}\cdot\boldsymbol{p}$ method; in $\boldsymbol{k}\cdot\boldsymbol{p}$ method with account of mass anisotropy; and with the valley splitting. States in D_3 NWs have the same structure as in D_{3d} without a certain parity.

A. Bulk Hamiltonian

The isotropic $\boldsymbol{k}\cdot\boldsymbol{p}$ Hamiltonian written in the basis of the spinors and the Bloch functions in the longitudinal valley L_0,

$$\boldsymbol{\mathcal{E}}_0 = \left(\left|L_0^c\right\rangle|\uparrow\rangle, \left|L_0^c\right\rangle|\downarrow\rangle, \left|L_0^v\right\rangle|\uparrow\rangle, \left|L_0^v\right\rangle|\downarrow\rangle\right), \tag{7}$$

takes the form [25,38,39]

$$H = \begin{bmatrix} \left(\frac{E_g}{2} - \alpha_c\Delta\right) & -iP(\boldsymbol{\sigma}\boldsymbol{\nabla}) \\ iP(\boldsymbol{\sigma}\boldsymbol{\nabla}) & -\left(\frac{E_g}{2} - \alpha_v\Delta\right) \end{bmatrix}, \tag{8}$$

where α_c,α_v are combinations of remote band mass parameters, P is the interband momentum matrix element.

In a bulk crystal with the inversion center chosen at a cation the conduction band Bloch function $|L_0^c\rangle$ is odd and the valence band Bloch function $|L_0^v\rangle$ is even, however, we use the $|L^{c,v}\rangle$ notation instead of commonly used $|L_0^{\mp}\rangle$ (or simply $|L^{\mp}\rangle$) because the parities of the Bloch functions depend on the position of the inversion center, which is different in D_{3d} and C_{2h} NWs, see Fig. 1.

It is worth noting that, for $k_z = 0$, the anisotropic model of Ref. [20] reduces to the isotropic one with renormalized parameters. Our $\boldsymbol{k}\cdot\boldsymbol{p}$ calculations will be limited to this case. The $\boldsymbol{k}\cdot\boldsymbol{p}$ parameters can be extracted from the band structure calculated using the tight-binding approach: $P^l = 3.8859\,\text{eV Å}$, $\alpha_c^l = 22.9078\,\text{eV Å}^2$, $\alpha_v^l = 27.5727\,\text{eV Å}^2$ for longitudinal valley L_0 and $P^i = 3.5943\,\text{eV Å}$, $\alpha_c^i = 15.9308\,\text{eV Å}^2$, $\alpha_v^i = 17.9751\,\text{eV Å}^2$ for inclined L_{123} valleys, with the zero-temperature band gap $E_g = 0.2129\,\text{eV}$.

B. Effective mass model for nanowire states originating from a single valley

Since the Hamiltonian Eq. (8) commutes with the total angular momentum operator $\hat{\boldsymbol{J}}$ [39], it is convenient to classify the NW's states with respect to its component, $\hat{J}_z$, along the growth direction. The eigenvalues of $\hat{J}_z$ are denoted by m. Equation (8) has four linearly independent solutions finite at $\rho = 0$, where ρ is the in-plane radial coordinate of the

cylindrical coordinate system. The boundary condition (which we choose in the form of vanishing wave functions at the surface of the nanowire) reduces the set to two.

For the states at the edges of the NW sub-bands ($k_z = 0$), one may obtain the following dispersion equation [25]:

$$g J_{m^+}(kR) I_{m^-}(\kappa R) - G J_{m^-}(kR) I_{m^+}(\kappa R) = 0, \tag{9}$$

where $J_{m^\pm}(kR)$, $I_{m^\pm}(\kappa R)$ are, respectively, Bessel and modified Bessel functions of the integer index $m^\pm = m \pm 1/2$, R is the NW radius,

$$\begin{aligned} g &= \frac{Pk}{\alpha_v k^2 + E + E_g/2}, \quad k = \sqrt{\Xi + \Lambda}, \\ G &= \frac{P\kappa}{\alpha_v \kappa^2 - E - E_g/2}, \quad \kappa = \sqrt{\Xi - \Lambda}, \end{aligned} \tag{10}$$

$$\Xi = \sqrt{\Lambda^2 + \frac{\left(4E^2 - E_g^2\right)}{4\alpha_v \alpha_c}},$$

$$\Lambda = \frac{E(\alpha_v - \alpha_c) - P^2 - (\alpha_v + \alpha_c)E_g/2}{2\alpha_v \alpha_c}. \tag{11}$$

For a given m, we enumerate all roots of the dispersion equation (9), $E_{m,n}$, with the index n in a way that a positive n refers to the nth positive root and a negative n refers to the $|n|$th negative root. For each energy, there exist two eigenfunctions of the Hamiltonian (8), which we denote as $|\nu = 0, \uparrow(\downarrow), m, n\rangle$. Below, for the sake of brevity, we will sometimes omit one or two of these indices, where it cannot lead to a confusion, but the order of the indices will always be preserved. The explicit form of the eigenfunctions is

$$|\uparrow(\downarrow), m\rangle = \boldsymbol{\mathcal{E}}_0 \, \hat{\mu}_{\uparrow(\downarrow),m}, \tag{12}$$

where $\boldsymbol{\mathcal{E}}_0$ is the row vector of the basis functions (7) and $\hat{\mu}_{\uparrow(\downarrow)m}$ are envelope column bispinors

$$\hat{\mu}_{\uparrow m} = \begin{pmatrix} u(\rho)e^{im^-\varphi} \\ 0 \\ 0 \\ i\,v(\rho)e^{im^+\varphi} \end{pmatrix}, \quad \hat{\mu}_{\downarrow m} = \begin{pmatrix} 0 \\ u(\rho)e^{-im^-\varphi} \\ i\,v(\rho)e^{-im^+\varphi} \\ 0 \end{pmatrix}, \tag{13}$$

where the radial functions $u(\rho)$, $v(\rho)$, are

$$\begin{aligned} u(\rho) &= N_m[J_{m^-}(k\rho) + c\, I_{m^-}(\kappa\rho)], \\ v(\rho) &= N_m[g J_{m^+}(k\rho) + c\, G I_{m^+}(\kappa\rho)], \end{aligned} \tag{14}$$

where $c = -J_{m^-}(kR)/I_{m^-}(\kappa R)$ and N_m is the normalization constant.

The functions Eq. (12), as mentioned above, are eigenfunctions of the $\hat{J}_z$ with the following eigenvalues

$$\hat{J}_z|\uparrow(\downarrow), m\rangle = \pm m|\uparrow(\downarrow), m\rangle. \tag{15}$$

Thus, the electron states at the nanowire sub-band edges ($k_z = 0$), originating from a single valley, are characterized by the main quantum number n, projection m of the total angular momentum on the NW axis, and parity. Numerical solutions of Eq. (9) for a few energies near the band gap are shown in Table I.

TABLE I. Sub-band-edge energies and quantum numbers for the first few sub-bands in the conduction and valence bands of a nanowire of the diameter 29.92 Å calculated in the framework of the isotropic $\boldsymbol{k}\cdot\boldsymbol{p}$ approximation with the two sets of parameters, listed in Sec. III A. Symmetries of the $\boldsymbol{k}\cdot\boldsymbol{p}$ states refer to the D_{3d} NWs and show distribution of the irreducible representations, S, associated with the states at the extrema of the corresponding energy sub-bands, over the longitudinal, L_0, and inclined, L_{123} valleys.

E_{L_0}, eV	S_{L_0}	$E_{L_{123}}$, eV	$S_{L_{123}}$	n	m
3.45	Γ_4^-	2.55	$\Gamma_{5,6}^- \oplus 2\Gamma_4^-$	2	$\frac{1}{2}$
3.04	$\Gamma_{5,6}^-$	2.27	$\Gamma_{5,6}^- \oplus 2\Gamma_4^-$	1	$-\frac{3}{2}$
2.99	Γ_4^-	2.21	$\Gamma_{5,6}^- \oplus 2\Gamma_4^-$	1	$\frac{5}{2}$
1.81	Γ_4^+	1.39	$\Gamma_{5,6}^+ \oplus 2\Gamma_4^+$	1	$-\frac{1}{2}$
1.77	$\Gamma_{5,6}^+$	1.34	$\Gamma_{5,6}^+ \oplus 2\Gamma_4^+$	1	$\frac{3}{2}$
0.81	Γ_4^-	0.65	$\Gamma_{5,6}^- \oplus 2\Gamma_4^-$	1	$\frac{1}{2}$
−0.94	Γ_4^+	−0.71	$\Gamma_{5,6}^+ \oplus 2\Gamma_4^+$	−1	$-\frac{1}{2}$
−2.08	$\Gamma_{5,6}^-$	−1.48	$\Gamma_{5,6}^- \oplus 2\Gamma_4^-$	−1	$-\frac{3}{2}$
−2.12	Γ_4^-	−1.53	$\Gamma_{5,6}^- \oplus 2\Gamma_4^-$	−1	$\frac{1}{2}$
−3.55	Γ_4^+	−2.46	$\Gamma_{5,6}^+ \oplus 2\Gamma_4^+$	−1	$-\frac{5}{2}$
−3.59	$\Gamma_{5,6}^+$	−2.51	$\Gamma_{5,6}^+ \oplus 2\Gamma_4^+$	−1	$\frac{3}{2}$
−4.09	Γ_4^+	−2.83	$\Gamma_{5,6}^+ \oplus 2\Gamma_4^+$	−2	$-\frac{1}{2}$

1. *Parity, T, and C symmetry of the states*

Taking into account the parity of the Bloch functions

$$\hat{P}\left(\left|L_0^c\right\rangle, \left|L_0^v\right\rangle\right) = \left(\left|L_0^c\right\rangle, \left|L_0^v\right\rangle\right)(-\sigma_z), \tag{16}$$

and the bispinor components, one can establish the parity of the eigenstates Eq. (12)

$$\hat{\mathbf{P}}|\uparrow(\downarrow), m\rangle = (-1)^{m^+}|\uparrow(\downarrow), m\rangle. \tag{17}$$

Without magnetic field, the $\boldsymbol{k}\cdot\boldsymbol{p}$ Hamiltonian commutes with the time-reversal operator $\hat{T}$, with the matrix form $(I_2 \otimes -i\sigma_y)\hat{K}_0$ in the basis Eq. (7). Here $\hat{K}_0$ is the complex conjugation operator and I_2 is the 2×2 unit matrix. Under the time reversal the eigenfunctions Eq. (12) transform one into another as spinors

$$\hat{T}(|\uparrow, m\rangle, |\downarrow, m\rangle) = (|\uparrow, m\rangle, |\downarrow, m\rangle)(-i\sigma_y). \tag{18}$$

Next we consider the charge conjugation operator [41] $\hat{C} = \gamma^2 \hat{K}_0$, where γ^μ are Dirac matrices [42], which act on the bispinors Eq. (13). The Hamiltonian (8) is not invariant under the C symmetry if $\alpha_c \neq \alpha_v$. The charge conjugated Hamiltonian is $H_C = -\gamma^2 H^* \gamma^2$, and the charge conjugation acting on the eigenfunctions produces functions, which do not satisfy the dispersion equations. However, if $\alpha_c = \alpha_v$ then charge conjugation reverses the sign of the Hamiltonian, $H_C = -H$, thus exchanging conduction and valence bands. In this case the main quantum number n changes its sign and the wave functions transform as

$$\hat{C}|\uparrow(\downarrow), m, n\rangle = \mathrm{sign}(n)(-1)^{m^-}|\uparrow(\downarrow), -m, -n\rangle. \tag{19}$$

We emphasize the fact that only in the case of a C-symmetric Hamiltonian the identity $E_{m,n} = -E_{-m,-n}$ holds. In contrast to the time-reversal operator $\hat{T}$, the charge conjugation operator $\hat{C}$ exchanges the states with the opposite

parity. Even though the charge symmetry does not hold in real lead chalcogenides, the corresponding analysis provides an insight into the structure of the electron energy levels. If one starts from the Hamiltonian with $\alpha_c = \alpha_v$, then the states can be classified using the charge conjugation operator. An adjustment of the parameters α_c, α_v to their actual values breaks the C symmetry, but this does not affect the degeneracies of the levels and only slightly changes their energy positions.

This analysis is helpful in revealing the relations between the solutions with positive and negative energies. In particular, it guarantees that negative energy solutions have the opposite parities with respect to the corresponding positive energy solutions.

2. *Point group symmetry of the states originating from the longitudinal valley*

In the previous section we characterized nanowire electron states, originating from a single valley of a bulk semiconductor, by the main quantum number n, projection m of the total angular momentum on the NW axis, and parity. This characterization assumes that the nanowire has an idealized shape of a circular cylinder, which implies the symmetry group $D_{\infty h}$, and does not take into account the fact that the symmetry of an actual nanowire is lower due to the underlying crystal structure. However, if one formally restricts the symmetry operations of the idealized nanowire by the symmetry operations of an actual nanowire point group, then one can assign an irreducible representation of this group to each electron energy level and thereby classify the states by their symmetry. In this paragraph we use this approach to analyze the symmetry of the states (12). It corresponds to the symmetry of the states originating from the longitudinal valley of a [111]-grown nanowire, which are decoupled from the states originating from all the other valleys.

The highest possible point group of an actual NW, $D_{3d} = D_3 \otimes C_i$ (cf. Fig. 1), has six spinor representations: $\Gamma_4^{\pm}$ and conjugated $\Gamma_5^{\pm}$ and $\Gamma_6^{\pm}$ [40]. Therefore, the electron states of a nanowire can transform either under $\Gamma_5^{\pm} \oplus \Gamma_6^{\pm}$ (below we denote them as $\Gamma_{5,6}^{\pm}$) or under $\Gamma_4^{\pm}$. In systems, where the z axis coincides with the C_3 symmetry axis, projection m of the angular momentum $\hat{J}_z$ is defined modulo 3. One may check that in our case this leads to the fact that the states (12) transform according to $\Gamma_{5,6}^{\pm}$ if $2m \bmod 3 = 0$ and $\Gamma_4^{\pm}$ otherwise. This result holds for the D_3 point group.

In case of C_{2h} NWs, there are four spinor representations. Two representations $\Gamma_3^{\pm}$ are conjugated to $\Gamma_4^{\pm}$ and the states transform either under $\Gamma_{3,4}^{+} \equiv \Gamma_3^{+} \oplus \Gamma_4^{+}$ or $\Gamma_{3,4}^{-}$. Parity analysis requires microscopic consideration and is discussed in the next section.

C. Effective mass model for combinations of valley states

In this section we extend the effective mass model to account for the valley structure of the states and classify the $\boldsymbol{k}\cdot\boldsymbol{p}$ solutions in accordance with the irreducible representations of the NW point group. In order to do that we introduce bases in form of Eq. (7) in each L_ν, ($\nu = 0,1,2,3$) valley

$$\mathcal{E}_\nu = \left(\left|L_\nu^c\right\rangle|\uparrow\rangle, \left|L_\nu^c\right\rangle|\downarrow\rangle, \left|L_\nu^v\right\rangle|\uparrow\rangle, \left|L_\nu^v\right\rangle|\downarrow\rangle\right) \tag{20}$$

and extend the set of solutions Eq. (12) of the isotropic $\boldsymbol{k}\cdot\boldsymbol{p}$ model by taking the valley index ν into account:

$$|\nu, \uparrow(\downarrow), m\rangle = \mathcal{E}_\nu\, \hat{\mu}_{\uparrow(\downarrow),\, m}. \tag{21}$$

To analyze the states Eq. (21) let us consider the wave vectors $\boldsymbol{k}_\nu$, ($\nu = 0,1,2,3$) of the L valleys Eq. (3). In the bulk point group O_h they form an irreducible star $S_{L_{0123}} = \{\boldsymbol{k}_\nu\}_{\nu=0}^{3}$, but lowering the symmetry to the point groups $D_{3d}^{[111]}$ or $D_3^{[111]} \subset O_h$ (C_3 axis points along the [111] direction) one can find that the star breaks into irreducible ones $S_{L_0} = \{\boldsymbol{k}_0\}$ and $S_{L_{123}} = \{\boldsymbol{k}_1, \boldsymbol{k}_2, \boldsymbol{k}_3\}$. In the $C_{2h}^{[111]} \subset D_{3d}^{[111]}$ the star $S_{L_{123}}$ further breaks into irreducible stars $S_{L_2} = \{\boldsymbol{k}_2\}$ and $S_{L_{13}} = \{\boldsymbol{k}_1, \boldsymbol{k}_3\}$. Within an irreducible star S the valley index ν transforms under rotation $\hat{g}$ as permutations of the wave vectors in the star, given by a matrix T_g: $\hat{g}\, S = S\, T_g$. This allows us to symmetrize the basis functions, Eq. (21), within the irreducible stars S_{L_0}, $S_{L_{123}}$ for D_{3d} and D_3 NWs and within S_{L_0}, S_{L_2}, $S_{L_{13}}$ for C_{2h} NWs.

Below we perform the symmetrization procedure only for the angular momentum $m = 1/2$, i.e., for the first confined electron states in each valley and we consider NWs with the groups D_{3d} and D_3 together.

1. *Valley structure of states in D_{3d} and D_3 NWs*

We have already shown in Sec. III B 2 that the states originating from the longitudinal valley (S_{L_0} star) in $D_{3(d)}$ NWs transform according to $\Gamma_4^{(-)}$, thus we consider only the star $S_{L_{123}}$, The wave vectors from this star transform under the rotations C_{3z} and C_{2x} according to the matrices:

$$T_{C_{3z}} = \begin{pmatrix} 0 & 0 & 1 \\ 1 & 0 & 0 \\ 0 & 1 & 0 \end{pmatrix}, \quad T_{C_{2x}} = \begin{pmatrix} 1 & 0 & 0 \\ 0 & 0 & 1 \\ 0 & 1 & 0 \end{pmatrix}. \tag{22}$$

This means that the wave vectors of the irreducible star $S_{L_{123}}$ form the basis of the $\Gamma_1^{(+)} \oplus \Gamma_3^{(+)}$ representation of the group $D_{3(d)}$. Taking spin into account, we can get a representation for the states associated with the irreducible star $S_{L_{123}}$ in $D_{3(d)}$ wires $(\Gamma_1^{(+)} \oplus \Gamma_3^{(+)}) \otimes \Gamma_4^{(-)} = \Gamma_{5,6}^{(-)} \oplus 2\Gamma_4^{(-)}$.

The states $\{|0,\uparrow,1/2\rangle, |0,\downarrow,1/2\rangle\}$ are chosen in such a way that their rotation matrices coincide with the corresponding spin rotation matrix $D_{1/2}(\boldsymbol{n},\omega) = \exp\left[-i\frac{\omega}{2}\boldsymbol{n}\boldsymbol{\sigma}\right]$, where $\boldsymbol{n}$ is the rotation axis direction and ω is the rotation angle. Taking into account the permutation matrices T, the full rotation matrices $D(g)$ for the states $\{|\nu,\uparrow\rangle, |\nu,\downarrow\rangle\}_{\nu=1}^{3}$ are Kronecker products of the matrices T and $D_{1/2}$: $D(g) = T_g \otimes D_{1/2}(g)$.

The symmetrization procedure for $D_{3(d)}$ NWs consists of a simultaneous diagonalization of the matrices $D(C_{3z})$ and $D(C_{2x})$. This can be achieved using the unitary matrix $V_{L_{123}}$ via $V^\dagger D V$. This matrix transforms the states as

$$\begin{aligned}&(|\Gamma_4^{(-)}\uparrow(\downarrow)\rangle, |\Gamma_4^{(-)}\uparrow(\downarrow)\rangle, |\Gamma_5^{(-)}\rangle, |\Gamma_6^{(-)}\rangle) \\ &\quad = (|1,\uparrow(\downarrow)\rangle, |2,\uparrow(\downarrow)\rangle, |3,\uparrow(\downarrow)\rangle) V_{L_{123}}.\end{aligned} \tag{23}$$

The explicit form of the matrix $V_{L_{123}}$ is

$$V_{L_{123}} = \begin{pmatrix} \frac{1}{\sqrt{3}} & 0 & 0 & \frac{i}{\sqrt{3}} & -\frac{i}{\sqrt{6}} & \frac{i}{\sqrt{6}} \\ 0 & \frac{1}{\sqrt{3}} & \frac{i}{\sqrt{3}} & 0 & \frac{i}{\sqrt{6}} & \frac{i}{\sqrt{6}} \\ \frac{1}{\sqrt{3}} & 0 & 0 & \frac{i\omega^2}{\sqrt{3}} & -\frac{i\omega}{\sqrt{6}} & \frac{i\omega}{\sqrt{6}} \\ 0 & \frac{1}{\sqrt{3}} & \frac{i\omega}{\sqrt{3}} & 0 & \frac{i\omega^2}{\sqrt{6}} & \frac{i\omega^2}{\sqrt{6}} \\ \frac{1}{\sqrt{3}} & 0 & 0 & \frac{i\omega}{\sqrt{3}} & -\frac{i\omega^2}{\sqrt{6}} & \frac{i\omega^2}{\sqrt{6}} \\ 0 & \frac{1}{\sqrt{3}} & \frac{i\omega^2}{\sqrt{3}} & 0 & \frac{i\omega}{\sqrt{6}} & \frac{i\omega}{\sqrt{6}} \end{pmatrix}, \tag{24}$$

where $\omega = \exp(\frac{2\pi i}{3})$. The phase choice guarantees that all the $\Gamma_4^{(-)}$ states transform as basis spinors $\{|\uparrow\rangle, |\downarrow\rangle\}$, and $\Gamma_5^{(-)}, \Gamma_6^{(-)}$ are coupled by the time reversal. The structure of the matrix $V_{L_{123}}$ enables one to analyze the valley structure of the states of a given symmetry. From (24) it follows that, for the $D_{3(d)}$ NWs, all the states with $m = 1/2$ originating from the inclined valleys are equally distributed over these valleys.

2. *Valley structure of states in C_{2h} nanowires*

The states in the third NW type with the point group C_{2h} are much easier to symmetrize than in the cases of the point groups D_{3d} and D_3. The C_{2h} point group contains only one nontrivial element: rotation around the $\boldsymbol{x}'$ axis $C_{2x'}$, which permutes wave vectors in the star $S_{L_{13}}$.

The states originating from the stars S_{L_0} and S_{L_2} can be symmetrized by the same matrix

$$(|\Gamma_3^-\rangle, |\Gamma_4^-\rangle) = (|0(2),\uparrow\rangle, |0(2),\downarrow\rangle) \begin{pmatrix} -\frac{\omega}{\sqrt{2}} & -\frac{\omega}{\sqrt{2}} \\ \frac{\omega^2}{\sqrt{2}} & -\frac{\omega^2}{\sqrt{2}} \end{pmatrix}. \tag{25}$$

The rest of the states originating from the star $S_{L_{13}}$ can be symmetrized as follows

$$(|\Gamma_3^+\rangle, |\Gamma_4^+\rangle, |\Gamma_3^+\rangle, |\Gamma_4^+\rangle) = (|1,\uparrow\rangle, |1,\downarrow\rangle, |3,\uparrow\rangle, |3,\downarrow\rangle) V_{L_{13}},$$

$$V_{L_{13}} = \frac{1}{2} \begin{pmatrix} -\omega^2 & \omega^2 & \omega^2 & \omega^2 \\ -\omega & -\omega & -\omega & \omega \\ 1 & -1 & 1 & 1 \\ 1 & 1 & -1 & 1 \end{pmatrix}. \tag{26}$$

One can see that the parity of the states at the $S_{L_{13}}$ star is opposite to the parity of the states at the S_{L_0} and S_{L_2} stars. The difference in parities arises from the parities of the atomic orbitals and the parity of the Bloch phase multiplier $e^{i\boldsymbol{kr}}$. In the case of the C_{2h} NWs, the inversion center is chosen at the point $a(\frac{1}{2}, \frac{1}{4}, \frac{1}{4})$ in the crystallographic coordinates (see Fig. 1), which changes the parities of the functions $|L_{1,3}^{c,v}\rangle$ to the opposite, as compared to the case when the inversion center is chosen at the (0,0,0) cation (the same as in bulk crystal), while keeping parities of the Bloch functions $|L_{0,2}^{c,v}\rangle$ the same.

IV. TIGHT-BINDING METHOD

In this section we discuss application of the empirical tight-binding method to PbSe nanowires. The tight-binding method is based on the expansion of the electron wave function $\Phi^s(\boldsymbol{r})$ in the local basis of atomiclike orbitals $\phi_\sigma(\boldsymbol{r})$, which are assumed to be orthogonal [43]:

$$\Phi^s(\boldsymbol{r}) = \sum_{n\sigma} C_{n\sigma}^s \phi_\sigma(\boldsymbol{r} - \boldsymbol{r}_n), \tag{27}$$

where n enumerates the atoms and the index σ runs through different orbitals. For the $sp^3d^5s^*$ variant of the method these are s, s^*, three p, and five d orbitals multiplied by spin-up and spin-down basis spinors, which results in the total of twenty orbitals per atom. In this basis, the Schrödinger equation reduces to the eigenvalue problem for a sparse matrix:

$$\sum_{n',\varsigma} H_{n\sigma,n'\varsigma} C_{n'\varsigma}^s = E_s C_{n\sigma}^s \,. \tag{28}$$

Here, the eigenvalues E_s correspond to the energies of the electron state s and eigenvectors $C_{n\sigma}$ provide the coefficients in the expansion (27) for this state. We use the nearest neighbor approximation, thus neglecting the matrix elements of the tight-binding Hamiltonian between the atoms that are not directly connected by a chemical bond. The explicit form of the Hamiltonian matrix elements, $H_{n\sigma,n'\varsigma}$, may be found in Refs. [44] or [45]. The spin-orbit interaction is introduced following Chadi [46]. The tight-binding parameters [33] are chosen to accurately reproduce experimental effective masses at the L point as well as the electron energies at the high-symmetry points of the Brillouin zone, which were calculated in Ref. [37] using the GW approximation.

For a nanowire, we introduce the wave vector K_z along the growth direction. Its relation to the wave vector k_z of Sec. III will become apparent later, in Sec. IV B. The tight-binding wave function for a NW takes the form

$$\Phi_{K_z}^s(\boldsymbol{r}) = \sum_{n\sigma} e^{iK_z z_n} C_{n\sigma}^s(K_z)\, \phi_\sigma(\boldsymbol{r} - \boldsymbol{r}_n), \tag{29}$$

where s is the band index, the index n runs over atoms in the elementary cell of the nanowire, and z_n is the z coordinate of the nth atom. Therefore, the tight-binding Hamiltonian for a nanowire is a finite matrix, which depends on the wave vector K_z and satisfies the equation

$$\sum_{n',\varsigma} H_{n\sigma,n'\varsigma}(K_z) C_{n'\varsigma}^s(K_z) = E_s(K_z) C_{n\sigma}^s(K_z) \,. \tag{30}$$

Its matrix elements are related to the matrix elements of the bulk Hamiltonian via $H_{n\sigma,n'\varsigma}(K_z) = e^{iK_z \delta z_{nn'}} H_{n\sigma,n'\varsigma}$, where $\delta z_{nn'}$ is the z component of the chemical bond vector between atoms n and n'.

The nanowire structures used in our tight-binding calculations can be conceived as being carved out from a bulk PbSe crystal and inscribed in a circular cylinder with the axis parallel to the [111] direction and passing through (i) an atomic site, (ii) the point with the coordinates $a/6(1,0,2)$, or (iii) the midpoint of a chemical bond, as shown in Fig. 1. We do not use surface passivation in our calculations. This is justified by the strong ionicity of the chemical bonds in the lead chalcogenides, which dramatically reduces the surface impact on the confined states [24,33,47] as compared to covalent semiconductors such as Si [48]. In realistic nanowires such passivation might be necessary to compensate for the unbalanced surface charge [49], however, its impact on the energy spectrum should be relatively weak.

TABLE II. Symmetry assignment for the eight low-energy conduction-band states obtained in the tight-binding calculations for NWs of three different symmetry groups.

Point group	Representation
D_{3d}	$3\Gamma_4^- \oplus \Gamma_{5,6}^-$
D_3	$3\Gamma_4 \oplus \Gamma_{5,6}$
C_{2h}	$2\Gamma_{3,4}^- \oplus 2\Gamma_{3,4}^+$

A. Point group symmetry

In order to analyze the symmetry of the tight-binding wave function one should determine how the symmetry operations, in particular rotations, affect the coefficients $C^s_{n\sigma}(K_z)$. First, a rotation causes the atoms to change their positions. Application of the group element g transforms the atom n with the coordinates $\boldsymbol{r}_n$ into the atom n' with the coordinates $\boldsymbol{r}_{n'} = g^{-1}\boldsymbol{r}_n$. This transformation is described by the permutation matrix P_g, which accumulates information about rotation of the atoms inside the NW. This matrix implicitly depends on the quasiwave vector K_z, as far as the transformations of the coefficients $C^s_{n\sigma}(K_z)$ are concerned.

Second, a rotation also affects the atomic orbitals forming the basis of the tight-binding Hamiltonian. Indeed, the $\pi/2$ rotation of the function p_x around z results in the function p_y which should be reflected in the corresponding change of the tight-binding coefficients. Formally, this may be described as follows. In the logic of the Slater-Koster notations [44] the s, p, and d functions transform as the basis functions of the momentum 0, 1, and 2, respectively. As a result, the action of the symmetry element g on these functions can be represented by Wigner's D matrices for these momenta. The tight-binding coefficients before and after a rotation operation g, are connected by the matrix $D_{\rm orb}(g)$:

$$D_{\rm orb}(g) = D_{1/2}(g) \otimes T^{-1} \begin{pmatrix} D_0^+(g) & & & \\ & D_1^-(g) & & \\ & & D_2^+(g) & \\ & & & D_0^+(g) \end{pmatrix} T, \tag{31}$$

where the matrix T transforms the spherical harmonics into the tesseral ones [50], which are used in tight-binding calculations [44,45].

The tight-binding coefficients before and after application of the symmetry operation g are connected by the matrix $D_{TB}(g)$, which is constructed as Kronecker's product of the permutation matrix P_g and the matrix $D_{\rm orb}(g)$:

$$D_{TB}(g) = P_g \otimes D_{\rm orb}(g)\,. \tag{32}$$

In the basis where the tight-binding Hamiltonian, $H_{n\sigma,n'\varsigma}(K_z)$, is diagonal, the transformation matrix (32) has a block-diagonal form, with the blocks corresponding to irreducible representations of the nanowire symmetry group. This allows us to associate the tight-binding wave functions with the irreducible representations of the NW symmetry group. The results of this procedure are presented for the eight low-energy conduction-band states in Table II. These results are in agreement with the symmetry analysis of Sec. III C.

B. Fourier analysis

In order to analyze how various states of the nanowire are related to different valleys of the bulk PbSe in the framework of the tight-binding method, we introduce the function

$$F^s_{K_z\omega}(\boldsymbol{\kappa}) = \sum_m e^{i(K_z z_m - \boldsymbol{\kappa}\boldsymbol{r}_m)} C^s_{m\omega}(K_z), \tag{33}$$

where s is the state index, the composite index ω labels both the sublattice (anions or cations) and the atomic orbitals, m enumerates atoms from one of the sublattices (specified in ω) within the elementary cell, $\boldsymbol{r}_m$ are the coordinates of these atoms, and z_m is the z component of $\boldsymbol{r}_m$. If the radius of the nanowire tends to infinity, $R \to \infty$, then the function (33) forms δ-like peaks near the projections of valley extrema onto the (111) plane and equivalent points in the reciprocal space. For NWs of finite radius, the width of the peaks depends on the NW radius as $\propto R^{-1}$.

The elementary cell of a nanowire contains six atomic layers in the planes perpendicular to the growth direction (cf. Fig. 1). The z coordinates of these layers, z_m, are 0, $a/\sqrt{3}$, and $2a/\sqrt{3}$ for the cation layers and $a/2\sqrt{3}$, $\sqrt{3}a/2$, and $5a/2\sqrt{3}$ for the anion layers. Taking this into account and substituting

$$\boldsymbol{\kappa} = K_z\,\hat{\boldsymbol{z}} + \boldsymbol{\kappa}_\rho + n\,\boldsymbol{b}_k, \tag{34}$$

where $\boldsymbol{\kappa}_\rho \perp \boldsymbol{z}$ and $n = 0,1,2$, one can rewrite Eq. (33) as

$$F^s_{K_z\omega}(\boldsymbol{\kappa}_\rho, n) = \sum_m e^{-i(\boldsymbol{\kappa}_\rho + \boldsymbol{b}_k\, n)\boldsymbol{r}_m} C^s_{m\omega}(K_z). \tag{35}$$

Here, K_z can assume any value within a one-dimensional Brillouin zone of the nanowire.

We further introduce the local density of states (LDOS) in the reciprocal space:

$$n^S_{K_z}(\boldsymbol{\kappa}_\rho, n) = \sum_{s\in S}\sum_\omega \left|F^s_{K_z\omega}(\boldsymbol{\kappa}_\rho, n)\right|^2, \tag{36}$$

where the index S refers to the set of states within one degenerate energy level. As in Sec. III C, we will be primarily interested in the states near the extrema of the nanowire energy sub-bands in the conduction and valence bands. Therefore, we set $K_z = k_0$ [cf. Fig. 1(d)]. and distinguish the three functions $n^S_{k_0}(\boldsymbol{\kappa}_\rho, 0)$, $n^S_{k_0}(\boldsymbol{\kappa}_\rho, 1)$, and $n^S_{k_0}(\boldsymbol{\kappa}_\rho, 2)$ corresponding to the three [111] planes in Fig. 1(d). We note that the quasi-wave-vectors K_z, used in this section, and k_z, used in Sec. III, are related by $k_z = K_z - k_0$. Therefore, the assignment of $K_z = k_0$ corresponds to $k_z = 0$.

As explained in Sec. II, the wave vectors from the first Brillouin zone of the bulk crystal, parallel to the [111] direction, which fill the interval $(-k_0, k_0]$ in the nanowire should be mapped onto the first Brillouin zone of the NW, which is three times smaller: $(-b_k/2, b_k/2]$ (zone folding). The number n in (35) allows for the unfolding of the band structure of the wire (see, e.g., Ref. [51]) onto the band structure of the bulk crystal. The use of all the three functions is superfluous, as they are connected by the translations

$$n^S_{k_0}(\boldsymbol{\kappa}_\rho, 0) = n^S_{k_0}(\boldsymbol{\kappa}_\rho - \boldsymbol{b}_1 + \boldsymbol{b}_k, 1) = n^S_{k_0}(\boldsymbol{\kappa}_\rho + \boldsymbol{b}_1 - \boldsymbol{b}_k, 2). \tag{37}$$

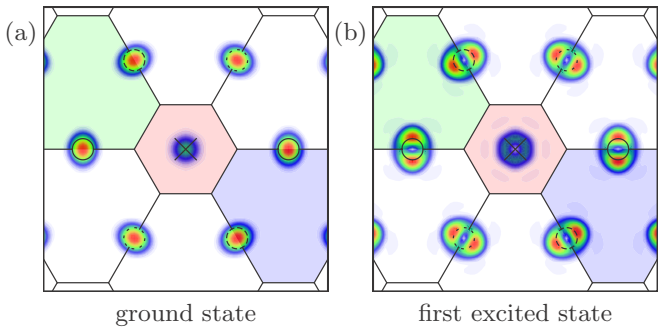

FIG. 3. LDOS in reciprocal space for the ground (a) and the first excited (b) conduction state in the D_{3d} NW with the 29.9 Å diameter.

Therefore, one can use only one of the planes in the valley analysis.

The analysis of the reciprocal space LDOS allows one to distinguish states of the same symmetry but with different main quantum numbers [52,53]. The reciprocal space LDOS for two levels with similar valley structure, but different main quantum numbers is illustrated in Fig. 3. Each reciprocal space maximum for the ground electron state corresponds to two maxima for the first excited state.

V. RESULTS

We have performed tight-binding calculations of energy spectra for NWs grown along [111] and having different symmetries. We will first present our results for the states at the extrema of the nanowire sub-bands as functions of the nanowire diameter. We will limit our consideration by the 24 states in the conduction and 24 states in the valence band. These states correspond to the three multiplets in each of the bands most close to the nanowire Fermi level (cf. Fig. 2). Each of the multiplets originates from an eightfold spin- and valley-degenerate level. These levels are first split into twofold and sixfold degenerate levels due to the effective mass anisotropy. When the valley mixing at the nanowire surface is taken into account then each of the eightfold degenerate levels is split into four doublets, see Fig. 2.

A. Valley structure

1. D_{3d} and D_3 NWs

First we discuss the D_{3d} nanowires. The states originating from the lowest-energy eightfold degenerate multiplet in the conduction band (see Fig. 2) form bases of $\Gamma^-_{5,6}$ and three Γ^-_4 irreducible representations. As discussed in Sec. III C, all the Γ^-_4 pairs of states have different LDOS in the reciprocal space. One pair has a significant amount of density near the longitudinal valley L_0 and the others have their densities mostly at the inclined valleys L_1, L_2, L_3 (see Fig. 5). Other multiplets are split into the states that transform according to the irreducible representations, see Table I.

The results of the calculations for six multiplets (three in the conduction and three in the valence band) are presented in Fig. 4. States transforming according to different irreducible representations are shown by crosses of different colors. This allows one to separate unambiguously the states originating from the $\boldsymbol{k}\cdot\boldsymbol{p}$ levels with $n=1, m=1/2$ from the pair of levels $n=1, m=-1/2,3/2$ since these levels have different parities (see Table I). An additional analysis is needed to reveal the valley structure of the levels because there are several sublevels with the same symmetry in all multiplets.

One can see that the valley splitting can exceed the energy distance between different multiplets for nanowire diameters below 40 Å. For instance, from the $\boldsymbol{k}\cdot\boldsymbol{p}$ theory one expects to

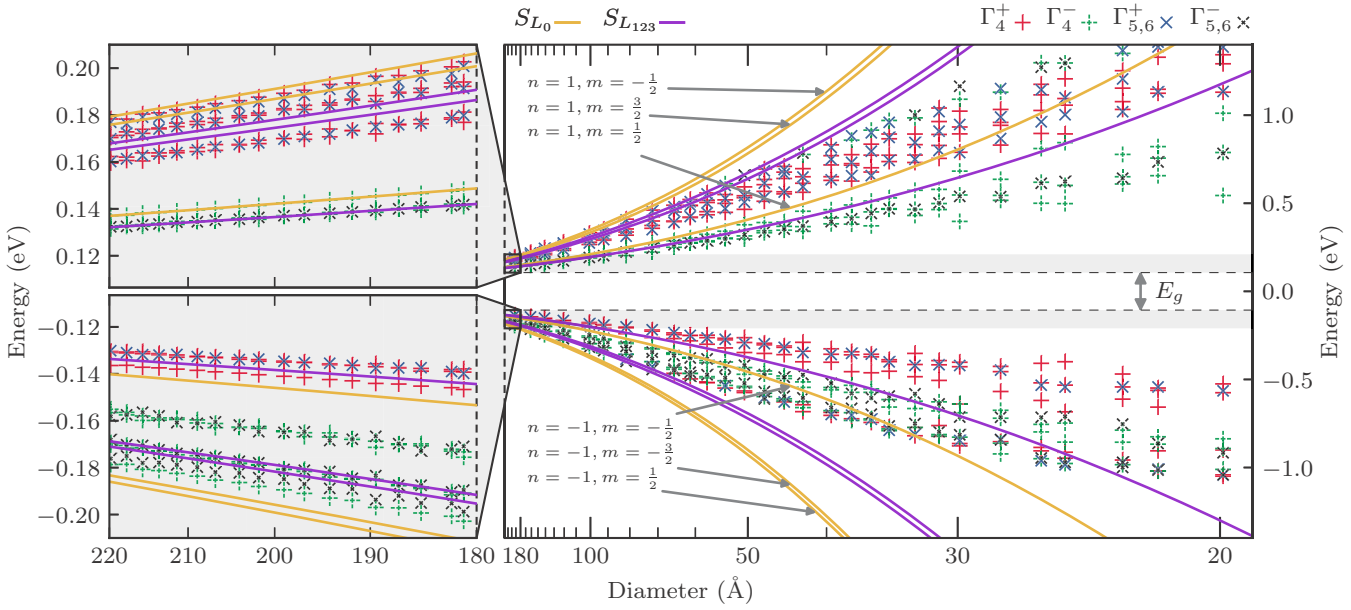

FIG. 4. Energy of the first 24 energy levels in the conduction and valence bands in D_{3d} nanowire as a function of the NW diameter. Tight-binding calculations are represented as colored symbols +'s and ×'s, encoding irreducible representations of states. The results of $\boldsymbol{k}\cdot\boldsymbol{p}$ calculations are shown by solid lines, purple for the inclined states, and yellow for the longitudinal ones. E_g is the band gap energy, arrangement of the $\boldsymbol{k}\cdot\boldsymbol{p}$ states is listed in Table I. Left panel shows a blow up of the region corresponding to large NW diameters.

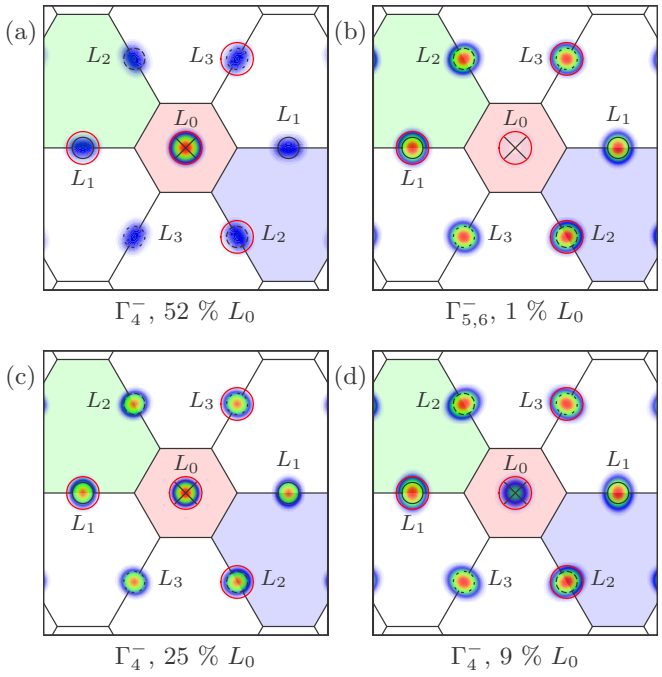

FIG. 5. Reciprocal space LDOS for four lowest-energy doublets of states in the conduction band of D_{3d} nanowire with the 29.9 Å diameter. The positions of the longitudinal valley L_0 are indicated by the cross and black circles (solid, dashed, dotted) show positions of the inclined valleys (L_1,L_2,L_3), see Sec. IV B. We also give the estimation (in percent) of L_0 valley contribution obtained by integration of the LDOS near the peaks (within the areas enclosed in red circles).

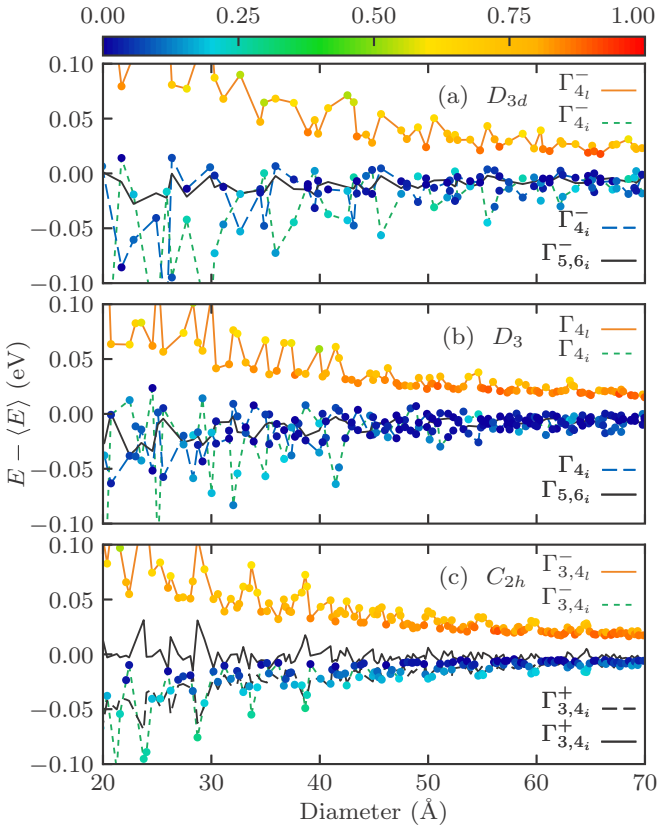

FIG. 6. Valley splittings for lowest conduction band states in (a) D_{3d}, (b) D_3, and (c) C_{2h} NWs as a function of the NW diameter. The colors of the dots encode the fraction of the longitudinal valley contribution L_0 to the confined state extracted from the $\boldsymbol{k}$-LDOS Eq. (36).

find in the conduction band four odd-parity doublets followed by eight even-parity doublets (see Table I). However, for some diameters, the highest-energy states shown in Fig. 4 have the odd parity and, therefore, originate from the odd-parity multiplets, which correspond to the top three lines of Table I. Thus, the intervalley coupling is comparable to the quantum confinement energy.

The strong intervalley coupling makes it impossible to track the origin of the states from the simple comparison with the $\boldsymbol{k} \cdot \boldsymbol{p}$ approximation, especially for the excited states. In order to resolve the valley structure of the ground-state multiplet, we use the analysis of reciprocal space LDOS explained in Sec. IV B.

In Fig. 5 we show the reciprocal space LDOS for the first four levels in the conduction band of a nanowire with the diameter 29.9 Å. In accordance with the symmetry analysis of Sec. III C, the level with the symmetry $\Gamma_{5,6}^-$ shows almost 100% fraction of the inclined valleys. This is expected because the corresponding states can mix only with the states of the same symmetry and there are no states of the same symmetry within the energy range ∼1 eV. There are also two levels of the symmetry Γ_4^-, which are combinations of the states of inclined valleys with a small admixture of the longitudinal valley L_0 and one level of the symmetry Γ_4^- with a strong admixture of the state from the longitudinal valley. The decomposition of the confined states over different valleys is clearly seen in Fig. 5.

The reciprocal space LDOS analysis can be used to trace the dependence of the valley splittings on the NW diameter. This dependence is highly oscillating, which is explained by the fact that even a small variation in the NW radius results in substantially different arrangements of the surface atoms, similar to the quantum dot case [32,33,54]. In Figs. 6(a)–6(c) we show only the first four double degenerate states in the conduction band for the NW diameters $16 \div 70$ Å for D_{3d} (a), D_3 (b), and C_{2h} (c) NWs. The energies in Fig. 6 are counted from the mean energy of the multiplet and are shown as functions of the nanowire diameter. The color of the points in Fig. 6 encodes the contributions of the longitudinal (L_0) and inclined ($L_{1,2,3}$) valleys to a given energy level. The red (blue) color corresponds to the predominant contribution of the longitudinal (inclined) valleys.

It is clearly seen that the valley composition strongly correlates with the levels repulsion. The more pure are the states of the Γ_4^- symmetry originating from the longitudinal and inclined valleys, respectively, the lower is the splitting between these valleys in Fig. 6(a). This correlation is somewhat obscured by the presence of the two levels originating from the inclined valleys. Below we will see that, for the NWs of the C_{2h} symmetry, it is more pronounced.

Next we briefly discuss the D_3 NWs, which have no inversion center. The dependences of energies of the confined

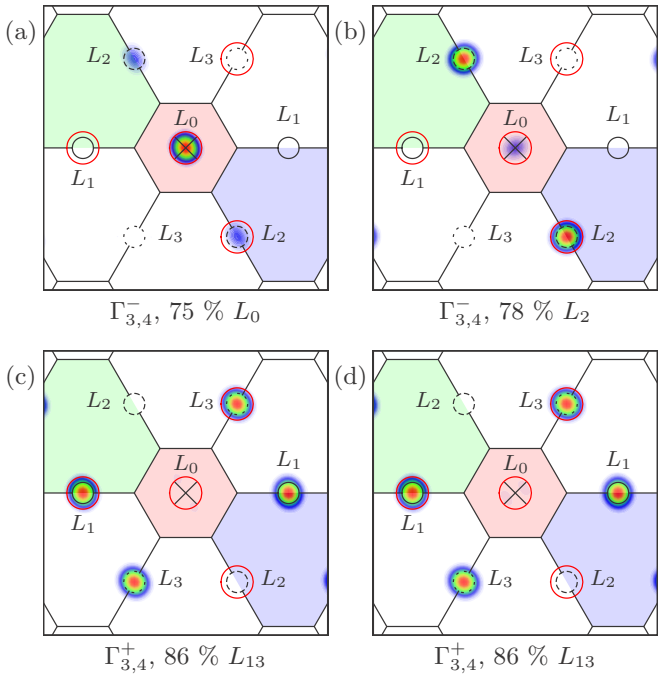

FIG. 7. Same as in Fig. 5, but for C_{2h} NW of diameter $D = 30.2$ Å.

states on the NW diameter are quite similar to these of the D_{3d} case presented in Fig. 4 and are not shown here. The valley splittings, shown in Fig. 6(b), oscillate with a somewhat smaller amplitude than in the D_{3d} case. This is probably due to a more symmetric surface of the D_{3d} NWs.

2. C_{2h} nanowires

The C_{2h} NWs are substantially different from the D_{3d} and D_3 NWs. The group C_{2h} has four spinor representations, $\Gamma_3^\pm$ and $\Gamma_4^\pm$, and all of them appear in the decomposition of the ground conduction (or valence) band state. The representations $\Gamma_3^\pm$ and $\Gamma_4^\pm$ are conjugate, and, therefore, the corresponding levels are doublets $\Gamma_{3,4}^\pm$. The fact that states of different parities originate from a single $\boldsymbol{k}\cdot\boldsymbol{p}$ level can be explained by the change in the position of the inversion center as compared to a bulk crystal. As shown in Sec. III C, the odd-parity states are formed by the states from the L_0 and L_2 valleys, while the even-parity states are formed by the states from the L_1 and L_3 valleys. This result can be also obtained in the framework of the tight-binding method, see Sec. IV A.

In Fig. 7 we show the reciprocal space LDOS for the first four levels in the conduction band of a nanowire with diameter 30.2 Å. Neglecting the valley mixing, the even-parity states $\Gamma_{3,4}^+$, originating from the valleys L_1 and L_3, are degenerate, while the odd-parity states $\Gamma_{3,4}^-$, originating from the L_0 and L_2 valleys, are split due to the valley anisotropy. Thus, it is natural to expect that the states originating from the $\boldsymbol{k}\cdot\boldsymbol{p}$ level $n = 1, m = 1/2$ with the symmetry $\Gamma_{3,4}^+$ are evenly distributed between the two valleys while each of the split $\Gamma_{3,4}^-$ levels are predominantly contributed by the states from either L_0 or L_2 valley. This qualitative analysis is in agreement with the calculated reciprocal space LDOS of the states presented in Fig. 7. The dependence of the first four levels in the conduction band on the nanowire diameter is shown in Fig. 6(c). For the odd-parity levels $\Gamma_{3,4}^-$, the valley composition strongly correlates with the levels repulsion. The larger is admixture of the L_2 valley to the state dominated by the L_0 valley (and vice versa), the stronger is the levels repulsion. Both levels exhibit strong oscillations with an amplitude up to 100 meV for small radii and decreasing with the NW radius. The strong correlation between the splitting of the levels and the degree of the valley admixture, encoded by the color in Fig. 6(c), clearly indicates that these oscillations are caused by the valley mixing at the interface.

B. Spin splitting

In Sec. V A we discussed the valley structure of different electron levels at the sub-band extrema for nanowires of different point groups. From the $\boldsymbol{k}\cdot\boldsymbol{p}$ analysis one could expect, that due to the spatial inversion in the bulk lead chalcogenides, it is impossible to obtain the fine spin structure of the energy levels in the nanostructures in the absence of magnetic field. We remind that the time-reversal symmetry together with the spacial inversion symmetry leads to the spin degeneracy of all levels

$$E_{\uparrow(\downarrow)m,n}(K_z) = E_{\uparrow(\downarrow)m,n}(-K_z). \tag{38}$$

However, the atomistic texture near the surface may break the spacial inversion, even in centrosymmetric materials [30,55] and this is the case of the NWs with the point group D_3. This group has no inversion center and Eq. (38) no longer holds for $K_z \neq 0$. Therefore, spin-dependent splittings of the states become possible. The spin splittings are linear in the wave vector K_z,

$$\Delta E^S_{\text{spin}} = \alpha_S(K_z - k_0) \equiv \alpha_S k_z, \tag{39}$$

where α_S is the splitting constant for the Sth couple of states. In Fig. 8 we show the energy dispersion curves for several lowest conduction band states for a D_3 NW of the diameter ≈40 Å. The Γ_4 ($\Gamma_5 \oplus \Gamma_6$) states are shown by the green (black) lines. In agreement with Eq. (39), the states exhibit linear-in-k spin

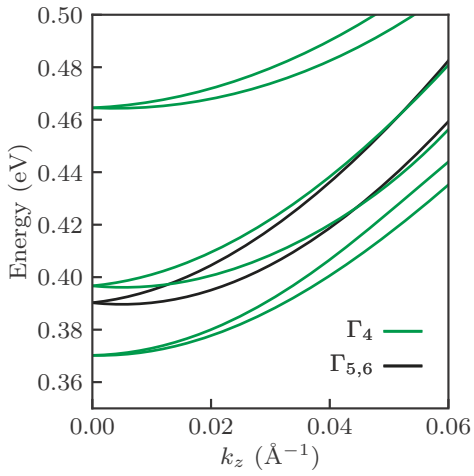

FIG. 8. Spin splittings of the ground conduction states in the D_3 NW with the 40 Å diameter. By green (black) lines we show Γ_4 ($\Gamma_{5,6}$) states. Wave vector k_z is measured from the band edge.

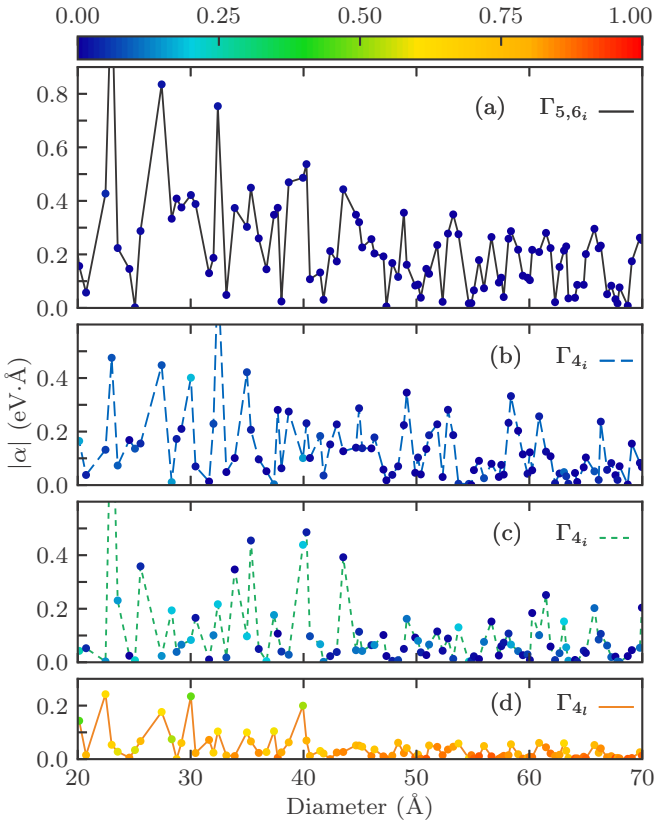

FIG. 9. Spin splittings of four conduction band doublets in NWs of D_3 symmetry as a function of the NW diameter. Color of the dots encodes the contribution of the longitudinal valley to the confined state.

splittings. The absolute values of α_S, extracted from the dispersion calculated in tight-binding technique, are shown in Fig. 9 as functions of the NW diameters for four lowest conduction band levels. Similar to the intervalley splittings, the constants of the spin splitting strongly oscillate with the NW radius.

Due to large atomic spin-orbit interaction constants [33]

$$\Delta_{\mathrm{Pb}} = 2.38\,\mathrm{eV}, \quad \Delta_{\mathrm{Se}} = 0.42\,\mathrm{eV},$$

and a narrow band gap, the spin splitting constants may be huge (up to 1 eV Å), as compared with typical values for A_3B_5 quantum wells [28,29,56,57]. Although a special design of A_3B_5-based nanowires [58] might lead to the same order of magnitude for the spin splitting, we stress that in our case we consider ideal nanowire of cylindrical shape based on material without bulk inversion asymmetry.

To make the spin splitting analysis complete, in Fig. 9 we show the spin splitting constants α_S as functions of the nanowire diameter. Each panel corresponds to a particular pair of states. The panels are sorted by the longitudinal valley contributions, encoded by the color of points in Fig. 9. One may note that the spin splitting is larger for the states with higher fractions of the inclined valleys.

VI. CONCLUSION

In this paper, we have calculated the energy spectrum of the [111]-grown PbSe nanowires in the framework of the empirical tight-binding method. By comparing the atomistic results with the $\boldsymbol{k}\cdot\boldsymbol{p}$ theory we demonstrated that the boundary scattering leads to the valley-orbit splitting of the confined states. The valley splitting of the energy levels is very sensitive to a particular arrangement of atoms in the nanowire. We have considered PbSe nanowires grown along the [111] direction with D_{3d}, D_3, and C_{2h} point group symmetry. Analysis of the local density of states in the reciprocal space allowed us to resolve the valley composition of the tight-binding wave functions. The strong correlation between the valley composition and the valley-orbit splittings shows that the main origin of the valley splitting is the intervalley mixing at the surface of the NW.

For relatively large nanowires with the diameters exceeding 40 Å the energy spectrum can be fairly well approximated in the framework of the $\boldsymbol{k}\cdot\boldsymbol{p}$ method, but for the diameters less than 40 Å the valley splittings of confined states become comparable with the energy distance between the unperturbed states from independent valleys and $\boldsymbol{k}\cdot\boldsymbol{p}$ theory should be modified to account for combinations of valley states.

The [111]-grown nanowires of the D_3 symmetry group represent a special case, as they lack inversion center and have a screw axis. For this reason they exhibit linear in wave vector spin-dependent splittings of energy levels. Our tight-binding calculations reveal giant spin splitting constants α up to 1 eV Å. This reflects the relativistic nature of electron spectrum in lead atoms and shows that the lead-chalcogenide nanowires are unexpectedly promising candidates for the spintronic devices. We believe that the intricate nature of the valley and spin splittings in small nanowires opens new opportunities in the control of spin and valley degrees of freedom.

ACKNOWLEDGMENTS

The authors acknowledge fruitful discussions with E. L. Ivchenko. The work of I.D.A., A.N.P., and M.O.N. was supported by the Russian Science Foundation (Grant No. 14-12-01067). The work of S.V.G. was supported by the National Science Foundation (NSF-CREST Grant No. HRD-1547754) and the Russian Foundation for Basic Research (Grant No. 15-02-09034).

[1] V. Sukhovatkin, S. Hinds, L. Brzozowski, and E. H. Sargent, Colloidal quantum-dot photodetectors exploiting multiexciton generation, Science **324**, 1542 (2009).

[2] E. H. Sargent, Infrared photovoltaics made by solution processing, Nature Photon. **3**, 325 (2009).

[3] O. E. Semonin, J. M. Luther, S. Choi, H.-Y. Chen, J. Gao, A. J. Nozik, and M. C. Beard, Peak external photocurrent quantum efficiency exceeding 100% via MEG in a quantum dot solar cell, Science **334**, 1530 (2011).

[4] J. M. Caruge, J. E. Halpert, V. Wood, V. Bulovič, and M. G. Bawendi, Colloidal quantum-dot light-emitting diodes with metal-oxide charge transport layers, Nature Photon. **2**, 247 (2008).

[5] L. Sun, J. J. Choi, D. Stachnik, A. C. Bartnik, B.-R. Hyun, G. G. Malliaras, T. Hanrath, and F. W. Wise, Bright infrared

quantum-dot light-emitting diodes through inter-dot spacing control, Nature Nanotechnol. **7**, 369 (2012).

[6] R. J. Ellingson, M. C. Beard, J. C. Johnson, P. Yu, O. I. Micic, A. J. Nozik, A. Shabaev, and A. L. Efros, Highly efficient multiple exciton generation in colloidal PbSe and PbS quantum dots, Nano Lett. **5**, 865 (2005).

[7] P. D. Cunningham, J. E. Boercker, E. E. Foos, M. P. Lumb, A. R. Smith, J. G. Tischler, and J. S. Melinger, Enhanced multiple exciton generation in quasi-one-dimensional semiconductors, Nano Lett. **11**, 3476 (2011).

[8] F. Gesuele, C. W. Wong, M. Sfeir, W.-k. Koh, C. B. Murray, and T. Heinz, Ultrafast supercontinuum spectroscopy of multiple exciton states in lead chalcogenide nanorods and nanocrystals, in *Conference on Lasers and Electro-Optics 2012* (Optical Society of America, San Jose, CA, USA, 2012) p. QM2G.2.

[9] L. A. Padilha, J. T. Stewart, R. L. Sandberg, W. K. Bae, W.-k. Koh, J. M. Pietryga, and V. I. Klimov, Aspect ratio dependence of Auger recombination and carrier multiplication in PbSe nanorods, Nano Lett. **13**, 1092 (2013).

[10] N. J. L. K. Davis, M. L. Böhm, M. Tabachnyk, F. Wisnivesky-Rocca-Rivarola, T. C. Jellicoe, C. Ducati, B. Ehrler, and N. C. Greenham, Multiple-exciton generation in lead selenide nanorod solar cells with external quantum efficiencies exceeding 120%, Nature Commun. **6**, 8259 (2015).

[11] H. Htoon, J. A. Hollingsworth, R. Dickerson, and V. I. Klimov, Effect of Zero- to One-Dimensional Transformation on Multiparticle Auger Recombination in Semiconductor Quantum Rods, Phys. Rev. Lett. **91**, 227401 (2003).

[12] J. Yang, B.-R. Hyun, A. J. Basile, and F. W. Wise, Exciton Relaxation in PbSe Nanorods, ACS Nano **6**, 8120 (2012).

[13] M. Aerts, F. C. M. Spoor, F. C. Grozema, A. J. Houtepen, J. M. Schins, and L. D. A. Siebbeles, Cooling and Auger recombination of charges in PbSe nanorods: Crossover from cubic to bimolecular decay, Nano Lett. **13**, 4380 (2013).

[14] E. Lifshitz, M. Bashouti, V. Kloper, A. Kigel, M. S. Eisen, and S. Berger, Synthesis and characterization of PbSe quantum wires, multipods, quantum rods, and cubes, Nano Lett. **3**, 857 (2003).

[15] K.-S. Cho, D. V. Talapin, W. Gaschler, and C. B. Murray, Designing PbSe nanowires and nanorings through oriented attachment of nanoparticles, J. Am. Chem. Soc. **127**, 7140 (2005).

[16] W.-k. Koh, A. C. Bartnik, F. W. Wise, and C. B. Murray, Synthesis of monodisperse PbSe nanorods: A case for oriented attachment, J. Am. Chem. Soc. **132**, 3909 (2010).

[17] B.-R. Hyun, A. C. Bartnik, W.-k. Koh, N. I. Agladze, J. P. Wrubel, A. J. Sievers, C. B. Murray, and F. W. Wise, Far-infrared absorption of pbse nanorods, Nano Lett. **11**, 2786 (2011).

[18] J. E. Boercker, E. E. Foos, D. Placencia, and J. G. Tischler, Control of PbSe nanorod aspect ratio by limiting phosphine hydrolysis, J. Am. Chem. Soc. **135**, 15071 (2013).

[19] D. Placencia, J. E. Boercker, E. E. Foos, and J. G. Tischler, Synthesis and optical properties of PbSe nanorods with controlled diameter and length, J. Phys. Chem. Lett. **6**, 3360 (2015).

[20] A. C. Bartnik, Al. L. Efros, W.-k. Koh, C. B. Murray, and F. W. Wise, Electronic states and optical properties of PbSe nanorods and nanowires, Phys. Rev. B **82**, 195313 (2010).

[21] J. E. Boercker, E. M. Clifton, J. G. Tischler, E. E. Foos, T. J. Zega, M. E. Twigg, and R. M. Stroud, Size and temperature dependence of band-edge excitons in PbSe nanowires, J. Phys. Chem. Lett. **2**, 527 (2011).

[22] P. D. Cunningham, J. E. Boercker, D. Placencia, and J. G. Tischler, Anisotropic absorption in PbSe nanorods, ACS Nano **8**, 581 (2014).

[23] L. A. Padilha, G. Nootz, S. Webster, D. J. Hagan, E. W. Van Stryland, L. Levina, V. Sukhovatkin, and E. H. Sargent, Two-photon absorption and multi-exciton generation in lead salt quantum dots, in *Ultrafast Phenomena in Semiconductors and Nanostructure Materials XIV*, edited by Jin-Joo Song, Kong-Thon Tsen, M. Betz, and A. Y. Elezzabi (SPIE, Bellingham, 2010).

[24] A. Paul and G. Klimeck, Atomistic study of electronic structure of PbSe nanowires, Appl. Phys. Lett. **98**, 212105 (2011).

[25] S. V. Goupalov, Comment on "electronic structure and optical properties of quantum-confined lead salt nanowires", Phys. Rev. B **84**, 037303 (2011).

[26] S. V. Goupalov, Finite-height effect on electron energy structure of lead salts nanorods, J. Phys. Chem. C **117**, 6476 (2013).

[27] F. J. Ohkawa, Electric break-through in an inversion layer: Exactly solvable model, Solid State Commun. **26**, 69 (1978).

[28] T. B. Boykin, G. Klimeck, M. Friesen, S. N. Coppersmith, P. von Allmen, F. Oyafuso, and S. Lee, Valley splitting in low-density quantum-confined heterostructures studied using tight-binding models, Phys. Rev. B **70**, 165325 (2004).

[29] T. B. Boykin, G. Klimeck, M. A. Eriksson, M. Friesen, S. N. Coppersmith, P. von Allmen, F. Oyafuso, and S. Lee, Valley splitting in strained silicon quantum wells, Appl. Phys. Lett. **84**, 115 (2004).

[30] M. O. Nestoklon, L. E. Golub, and E. L. Ivchenko, Spin and valley-orbit splittings in SiGe/Si heterostructures, Phys. Rev. B **73**, 235334 (2006).

[31] J. M. An, A. Franceschetti, and A. Zunger, The excitonic exchange splitting and radiative lifetime in pbse quantum dots, Nano Lett. **7**, 2129 (2007).

[32] R. Rahman, J. Verduijn, N. Kharche, G. P. Lansbergen, G. Klimeck, L. C. L. Hollenberg, and S. Rogge, Engineered valley-orbit splittings in quantum-confined nanostructures in silicon, Phys. Rev. B **83**, 195323 (2011).

[33] A. N. Poddubny, M. O. Nestoklon, and S. V. Goupalov, Anomalous suppression of valley splittings in lead salt nanocrystals without inversion center, Phys. Rev. B **86**, 035324 (2012).

[34] E. O. Wrasse, R. J. Baierle, T. M. Schmidt, and A. Fazzio, Quantum confinement and spin-orbit interactions in PbSe and PbTe nanowires: First-principles calculation, Phys. Rev. B **84**, 245324 (2011).

[35] E. O. Wrasse, R. J. Baierle, A. Fazzio, and T. M. Schmidt, First-principles study of group III impurity doped PbSe: Bulk and nanowire, Phys. Rev. B **87**, 085428 (2013).

[36] K. Hummer, A. Grüneis, and G. Kresse, Structural and electronic properties of lead chalcogenides from first principles, Phys. Rev. B **75**, 195211 (2007).

[37] A. Svane, N. E. Christensen, M. Cardona, A. N. Chantis, M. van Schilfgaarde, and T. Kotani, Quasiparticle self-consistent *GW* calculations for PbS, PbSe, and PbTe: Band structure and pressure coefficients, Phys. Rev. B **81**, 245120 (2010).

[38] J. O. Dimmock and G. B. Wright, Band edge structure of PbS, PbSe, and PbTe, Phys. Rev. **135**, A821 (1964).

[39] I. Kang and F. W. Wise, Electronic structure and optical properties of PbS and PbSe quantum dots, J. Opt. Soc. Am. B **14**, 1632 (1997).

[40] G. F. Koster, J. O. Dimmock, R. G. Wheeler, and H. Statz, *The Properties of the Thirty-Two Point Groups* (M.I.T. Press, Cambridge, 1963).

[41] V. B. Berestetskii, E. M. Lifshitz, and L. P. Pitaevskiĭ, *Quantum Electrodynamics*, Course of theoretical physics (Butterworth-Heinemann, Oxford, 1982).

[42] J. D. Bjorken and S. D. Drell, *Relativistic Quantum Fields* (Dover Publications, Mineola, 2013).

[43] P.-O. Löwdin, On the non-orthogonality problem connected with the use of atomic wave functions in the theory of molecules and crystals, J. Chem. Phys. **18**, 365 (1950).

[44] J. C. Slater and G. F. Koster, Simplified LCAO method for the periodic potential problem, Phys. Rev. **94**, 1498 (1954).

[45] A. V. Podolskiy and P. Vogl, Compact expression for the angular dependence of tight-binding Hamiltonian matrix elements, Phys. Rev. B **69**, 233101 (2004).

[46] D. J. Chadi, Spin-orbit splitting in crystalline and compositionally disordered semiconductors, Phys. Rev. B **16**, 790 (1977).

[47] G. Allan and C. Delerue, Confinement effects in PbSe quantum wells and nanocrystals, Phys. Rev. B **70**, 245321 (2004).

[48] C. Delerue and M. Lannoo, *Nanostructures. Theory and Modelling* (Springer Verlag, Berlin, 2004).

[49] R. Leitsmann and F. Bechstedt, Characteristic energies and shifts in optical spectra of colloidal IV-VI semiconductor nanocrystals, ACS Nano **3**, 3505 (2009).

[50] E. T. Whittaker and G. N. Watson, *A Course of Modern Analysis* (Watchmaker Publishing, Aberdeen, 2012).

[51] T. B. Boykin, A. Ajoy, H. Ilatikhameneh, M. Povolotskyi, and G. Klimeck, Unfolding and effective bandstructure calculations as discrete real- and reciprocal-space operations, Physica B **491**, 22 (2016).

[52] K. Dohnalová, A. N. Poddubny, A. A. Prokofiev, W. D. A. M. de Boer, C. P. Umesh, J. M. J. Paulusse, H. Zuilhof, and T. Gregorkiewicz, Surface brightens up Si quantum dots: direct bandgap-like size-tunable emission, Light: Science & Applications **2**, e47 (2013).

[53] P. Hapala, K. Kůsová, I. Pelant, and P. Jelínek, Theoretical analysis of electronic band structure of 2- to 3-nm Si nanocrystals, Phys. Rev. B **87**, 195420 (2013).

[54] M. Friesen and S. N. Coppersmith, Theory of valley-orbit coupling in a Si/SiGe quantum dot, Phys. Rev. B **81**, 115324 (2010).

[55] M. O. Nestoklon, E. L. Ivchenko, J.-M. Jancu, and P. Voisin, Electric field effect on electron spin splitting in SiGeSi quantum wells, Phys. Rev. B **77**, 155328 (2008).

[56] B. Jusserand, D. Richards, H. Peric, and B. Etienne, Zero-Magnetic-Field Spin Splitting in the Gaas Conduction Band from Raman Scattering on Modulation-Doped Quantum Wells, Phys. Rev. Lett. **69**, 848 (1992).

[57] M. O. Nestoklon, S. A. Tarasenko, R. Benchamekh, and P. Voisin, Spin splitting of electron states in lattice-mismatched (110)-oriented quantum wells, Phys. Rev. B **94**, 115310 (2016).

[58] A. A. Soluyanov, D. Gresch, M. Troyer, R. M. Lutchyn, B. Bauer, and C. Nayak, Optimizing spin-orbit splittings in insb majorana nanowires, Phys. Rev. B **93**, 115317 (2016).